Geophys. J. Int. () , 1–**??**

Cross-section electrical resistance tomography of La Soufrière of Guadeloupe lava dome

Nolwenn Lesparre[1⋆], Bartłomiej Grychtol[2], Dominique Gibert[3,4], Jean-Christophe Komorowski[3], Andy Adler[1]

[1] *Systems and Computer Engineering, Carleton University, Ottawa, Canada*
[2] *Medical Physics in Radiology, German Cancer Research Center, Heidelberg, Germany*
[3] *Institut de Physique du Globe de Paris, Sorbonne Paris Cité, Univ Paris Diderot, UMR 7154 CNRS, Paris, France.*
[4] *Géosciences Rennes, Univ Rennes 1, UMR 6118 CNRS, Rennes, France.*

SUMMARY

The electrical resistivity distribution at the base of La Soufrière of Guadeloupe lava dome is reconstructed by using transmission electrical resistivity data obtained by injecting an electrical current between two electrodes located on opposite sides of the volcano. Several pairs of injection electrodes are used in order to constitute a data set spanning the whole range of azimuths, and the electrical potential is measured along a cable covering an angular sector of $\approx 120^\circ$ along the basis of the dome. The data are inverted to perform a slice electrical resistivity tomography (SERT) with specific functions implemented in the EIDORS open source package dedicated to electrical impedance tomography applied to medicine and geophysics. The resulting image shows the presence of highly conductive regions separated by resistive ridges. The conductive regions correspond to unconsolidated material saturated by hydrothermal fluids. Two of them are associated with partial flank collapses and may represent large reservoirs that could have played an important role during past eruptive events. The resistive ridges may represent massive andesite and are expected to constitute hydraulic barriers.

Key words: Electrical properties – tomography – image processing – Volcanic hazards and risks

1 INTRODUCTION

La Soufrière of Guadeloupe volcano belongs to the active part of the volcanic arc forming the Lesser Antilles and caused by the subduction of the North American plate beneath the Caribbean plate. The La Soufrière lava dome (Fig. 1) is dated 1530 A.D. (Boudon *et al.*, 2008) and constitutes the most recent and presently single active part of La Découverte volcano complex (Samper *et al.*, 2009). Over the last $12,000$ years this area has been subject to intense magmatic activity marked by a series of dome extrusions, explosive eruptions, and partial edifice collapses. At least 8 such events occurred during the last 7800 years (Komorowski *et al.*, 2005; Komorowski *et al.*, 2008; Legendre, 2012).

La Soufrière lava dome is located in the horseshoe-shaped *Amic* crater formed 3100 B.P. by a St. Helens-type edifice collapse and directed blast event (Boudon *et al.*, 1987). Since its formation, La Soufrière had 6 phreatic eruptions (1690, $1797-1798$, $1809-1812$, $1836-1837$, 1956, $1976-1977$) located in different sectors of the northern and eastern sides of the lava dome (Fig. 2). The last $1976-1977$ event is considered a failed magmatic eruption (Feuillard *et al.*, 1983; Komorowski *et al.*, 2005; Villemant *et al.*, 2005; Boichu *et al.*, 2008; Boichu *et al.*, 2011) caused by the intrusion of a small volume of andesitic magma whose ascension stopped at about 3 km beneath the dome summit (Villemant *et al.*, 2005; Boichu *et al.*, 2011). Since then, this magma body sporadically releases acid gases in the hydrothermal reservoirs and produces episodic chlorine spikes in the *Carbet* hot spring located on the north-east side of the volcano (Boichu *et al.*, 2011). The thermal energy released in the shallower parts of the volcano drove thermal convection of hydrothermal fluids. This crisis was particularly intense and forced the evacuation of $73,000$ inhabitants over 6 months.

⋆ Now at: PRP-DGE Department, Institute for Radiological Protection and Nuclear Safety, B.P. 17, 92262 Fontenay-aux-Roses Cedex, France.

Figure 1. La Soufrière lava dome seen from North-East. The dashed line marks the Eastern segment of the electrode line shown in Fig. 2. The small landslide visible on the picture is located in front of the $C2$ conductive region of Fig. 8, and the blue arrows mark two lahars that occurred during the $1976-1977$ crisis in front of the $C3$ conductive region (see also Figs 8 and 9). The CS and GT labels respectively point the South Crater and the Tarissan pit locations (green points in Fig. 2).

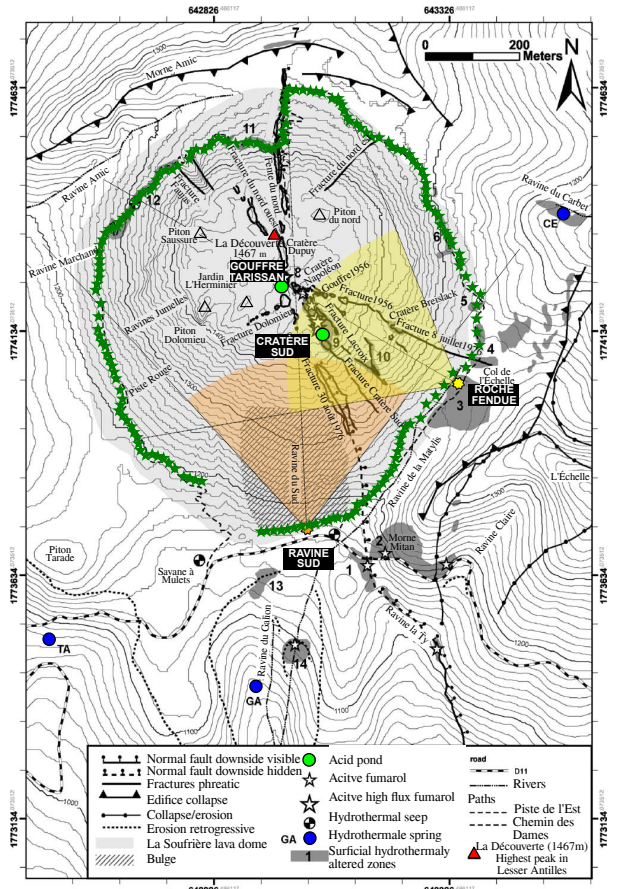

Figure 2. Map of the location of the main structures, historical eruptive vents, and sites of currently observed fumarolic activity on La Soufrière lava dome (Komorowski, 2008). The area corresponding to the lava dome is represented in light grey. The positions of the electrodes used in this study are indicated by green stars; see Fig. 4 for electrical current patterns. The sites of telescopes deployed for muon radiography (Fig. 3) are indicated by the yellow and orange stars. The telescopes' line of sight and angular aperture are also indicated.

Following the $1976-1977$ crisis, both the volcanic and seismic activities reduced gradually until 1992 when a noticeable increase in shallow low-energy seismicity and in the flux of summit fumarolic activity was observed (Komorowski *et al.*, 2005). One possible interpretation of this event is attributed to a reorganization of the fluid circulation pattern inside the lava dome as a response to progressive sealing of the hitherto active flow-paths. Both the intense hydrothermal activity and the heavy rains ($\approx 5\,\mathrm{m/year}$) supplying the hydrothermal shallow reservoirs favour fluid mineralization by magmatic gas and the formation of clayey material that progressively fills and blocks open fractures in the edifice decreasing its macro permeability (Zlotnicki *et al.*, 1994; Villemant *et al.*, 2005; Salaün *et al.*, 2011). The resulting sealing causes fluid confinement and over-pressurization that eventually leads to the opening of new flow paths inside the edifice (Salaün *et al.*, 2011). Another possibility is that this seismic and fumarolic reactivation characterized with a new pulse of marked chlorine degassing reflects injections of magmatic fluids and heat from the magmatic reservoir to some shallower level in the hydrothermal system below the summit (Fournier, 2006).

The past eruptive history of La Soufrière indicates that somewhat different scenarios have to be considered for the future, depending on the nature of the event: collapse, phreatic eruption, magma ascent (Komorowski *et al.*, 2008). The evaluation of hazards for each scenario depends on both the impact and the likelihood of each type of event, and some of them suggest important societal impacts in case of renewed activity. For this reason, multi-parameter monitoring is conducted by the local volcano observatory (IPGP/OVSG). Permanent networks monitor seismicity and ground deformation. Thermal springs and fumaroles are also sampled and analysed on a fortnightly base (Villemant *et al.*, 2005). Beside these routine measurements, it is important to perform complementary geophysical studies to obtain an ever more precise view of the inner structure of the volcano and derive models necessary to better understand the monitoring data. Knowledge of the inner structure is necessary to set reliable initial conditions to flank destabilization models (Le Friant *et al.*, 2006) and to estimate the amount of fluid contained in shallow hydrothermal reservoirs that may supply thermal and explosive energy in case of phreatic explosion and provoke lahars as observed during the $1976-1977$ crisis.

Over the last decade, La Soufrière of Guadeloupe has been subject to several geophysical imaging experiments including self-potential mapping (Zlotnicki *et al.*, 1994), electrical resistivity (Nicollin *et al.*, 2006), very low frequency survey (Zlotnicki *et al.*, 2006). Such methods were particularly sensitive to the presence of fluids circulating in the volcano hydrothermal system. The self-potential study evidenced the structural heterogeneity of La Soufrière lava dome and the circulation of fluids (Zlotnicki *et al.*, 1994). Negative anomalies present on the northern part of the dome emphasized the presence of vertical conduits where meteoric fluids circulated mostly downward (Zlotnicki *et al.*, 1994). A smooth positive anomaly enclosed the dome (except on the north-western part) and underlined the crater Amic wall

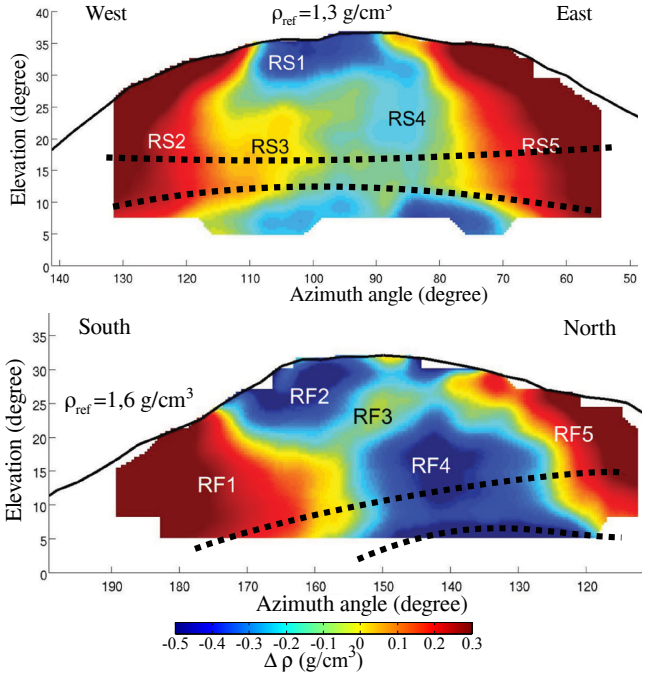

Figure 3. Density radiographies obtained with cosmic muon telescopes placed at the *Ravine Sud* (top) and *Roche Fendue* (bottom) locations (Lesparre *et al.*, 2012). Locations and angular ranges spanned by the radiographies are shown in Fig. 2: the *Ravine Sud* radiography is roughly West-East oriented, and the *Roche Fendue* is oriented South-North. The regions of the radiographies contained between the doted lines correspond to radiography rays (see appendix A for details) passing through the SERT cross-section limited by the electrode ring in Fig. 5.

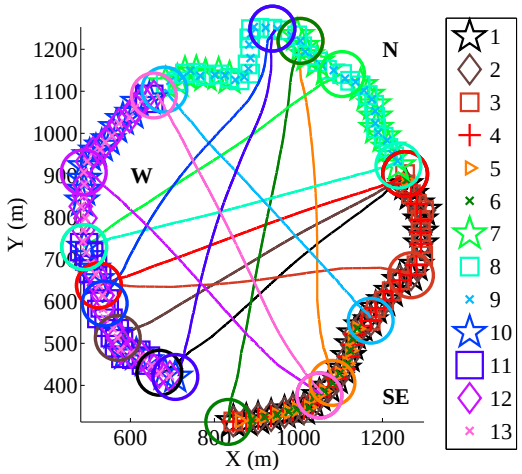

Figure 4. Map showing the 13 pairs of current electrodes (circles) used in the present study. The curved lines crossing the volcano correspond to the main current lines (calculated using a 2D homogeneous model) joining the corresponding current electrodes. The electrodes used for acquisitions are represented with different symbols and colours that correspond to a specific pair of stimulating electrodes represented by circles.

and was correlated to ancient or active fumarolic areas, signalling the existence of upward flowing fluids (Zlotnicki *et al.*, 1994). The VLF survey (Zlotnicki *et al.*, 2006) allowed to characterize the state of the main fault systems located on the volcano: hydrothermally active faults appear electrically conductive, and clayed, sealed or opened faults have higher resistivity values (Zlotnicki *et al.*, 2006). Profiles of apparent electrical resistivity display high resistivity contrasts confirming the heterogeneous structure of the dome (Nicollin *et al.*, 2006). Some profiles also indicate the presence of vertical conductive conduits interpreted as paths of an upward circulation for hydrothermal fluids. Local 1D geo-electrical soundings (Nicollin *et al.*, 2006) show that highly conductive material surrounds the dome and could constitute a continuous layer below the basis of the dome.

The dome density distribution was also studied using gravity measurements (Gunawan, 2005) jointly inverted with seismic data (Coutant *et al.*, 2012). These studies confirmed the heterogeneous structure of the dome. Recently, a cosmic muon radiography method has been developed (Gibert *et al.*, 2010; Lesparre *et al.*, 2010; Marteau *et al.*, 2012) and applied to La Soufrière lava dome (Lesparre *et al.*, 2012) to perform direct imaging of its density structure (Fig. 3, see appendix A for details). The resulting radiographies agrees with previous observations and clearly show low density hydrothermally altered regions.

The aim of the present study is to contribute to the knowledge of the lava dome interior by performing a slice electrical resistivity tomography (SERT) obtained by inverting an electrical resistivity data set acquired in December 2003 as a by-product of the global geo-electrical survey presented by Nicollin *et al.* (2006). The data set considered here was acquired with a transmission tomography configuration in order to probe the innermost regions of the lava dome.

2 SLICE ELECTRICAL RESISTIVITY TOMOGRAPHY (SERT)

2.1 Data

The data analysed in the present study constitute a subset of so far unprocessed measurements acquired during a larger electrical resistivity survey performed in December 2003 (Nicollin *et al.*, 2006). The data were acquired with a multi-electrode resistivity meter connected to a 945 m long main cable equipped with 64 plugs connected to stainless-steel electrodes. Either plug 1 or 64 located at the extremities of the main cable is connected to an auxiliary long wire in order to place the corresponding electrode on the opposite side of the lava dome. Both the remote electrode and one electrode plugged onto the main cable are used to inject an electrical current forced to cross the innermost parts of the volcano (Fig. 4). The main cable was moved to successively occupy three circular segments, each of them covering about one third of La Soufrière circumference to form an almost closed loop (Fig. 4). The entire data set counts a total of 298 measurements obtained with 13 pairs of current electrodes combined with a number of pairs of potential electrodes that varies between 12 and 30 (Table 1). The maximal distance between current electrodes is of 940 m in the North-South direction and of 820 m in the East-West direction. The electrode positions fall nearby a slightly inclined plane with an elevation decrease of 230 m from North to South (Fig. 5). The elevations of the electrode loop vary between 1146 and 1337 m with an average of 1270 m, *i.e.* about 200 m bellow the summit.

The primary data set is formed by $K = 298$ n-tuples $\{I_k, V_k, C_k^-, C_k^+, P_k^-, P_k^+\}$ where I_k is the electrical current

Table 1. Description of the measuring electrodes configuration for each pair of stimulating electrodes.

Current electrode pair	Main cable location	Profile length (m) measurements	Mean distance between V electrodes (m)	Number of V electrodes dipoles
1	SE	851	29	29
2	SE	851	29	29
3	SE	836	56	15
4	SE	841	30	28
5	SE	784	56	14
6	SE	754	54	14
7	N	788	39	20
8	N	850	28	30
9	N	842	28	30
10	W	849	39	21
11	W	733	61	12
12	W	854	33	26
13	W	831	28	30

for current electrode positions C_k^-, C_k^+ and V_k is the voltage measured between electrodes P_k^-, P_k^+. The current was automatically adjusted between 20 and 100 mA to ensure good signal-to-noise ratio. More details concerning the measurement procedure are given by Nicollin *et al.* (2006), and a discussion about the assessment of the data quality may be found in Nicollin et al. (2007). The noise presents in the data is mainly multiplicative with an estimated signal-to-noise ratio of about 90%.

Since the distance between the potential electrodes may greatly vary from one n-tuple to another, V_k spans several orders of magnitude. Consequently, a normalisation is performed by converting the $\{I_k, V_k\}$ pairs into apparent resistivity $\rho_{app,k} = \beta_k V_k / I_k$ (Fig. 6) where the geometrical factor β_k is computed with a 3D model of the volcano (Fig. 5) (Lesparre *et al.*, 2013). The resulting apparent resistivities

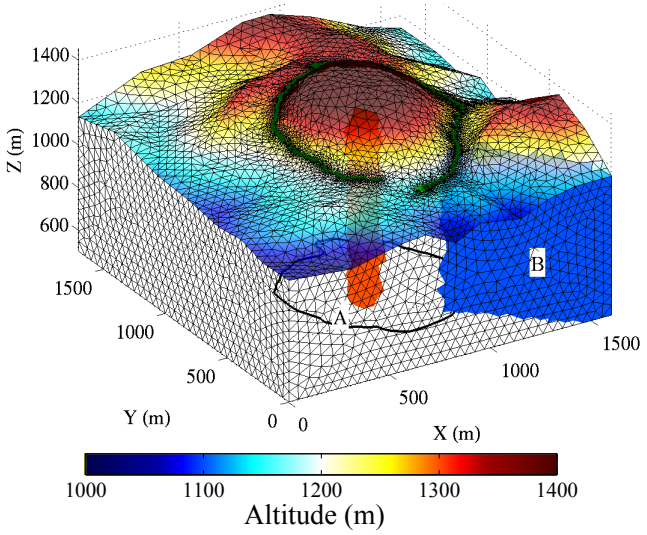

Figure 5. Finite element model used to compute the forward problem. x and y coordinates are oriented positively eastward and northward respectively. The orange vertical column (A) is obtained through a vertical extrusion of the elements (A) in Fig. 7. The blue elements (B) located in the exterior domain of the cross-section are obtained through a combination of vertical extrusion and a nearest neighbour extrapolation of elements B in Fig. 7.

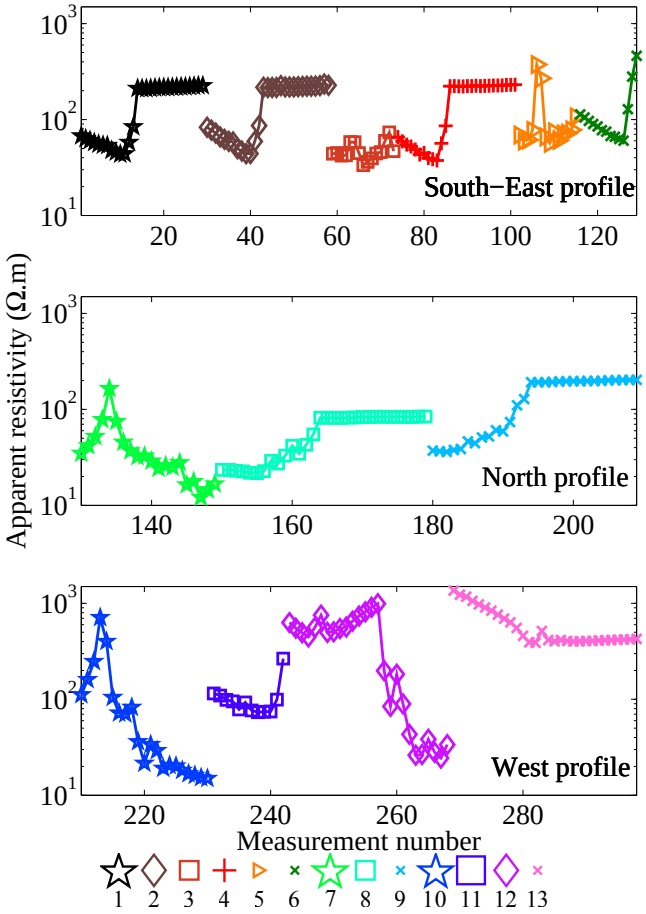

Figure 6. Apparent resistivity acquired from the different electrode profiles surrounding the dome. Colours correspond to the configuration number given in Fig. 4 and table 1.

vary between 12 and 1360 Ω.m. These values agree with the pseudo-sections obtained by Nicollin *et al.* (2006) where the apparent resistivites are mainly comprised in the 10 and 2000 Ω.m range. Apparent resistivities up to 10,000 Ω.m are reported by these authors for several shallow areas where massive andesitic rock and cavities are present. Because of the particular electrode set-up used in the present study, these shallow high-resistivity regions are not expected to significantly influence our data which are aimed to mainly sample the innermost parts of the lava dome. Discrepancies between the apparent resistivites derived in the present study and those obtained by Nicollin *et al.* (2006) may also be partly explained by the fact that these authors used a flat geometry to compute their geometrical factors instead of a full 3D model like in the present study (Fig. 5).

2.2 SERT inversion

The limited amount of data available is not suitable to perform a full 3D reconstruction of the conductivity structure inside the volcano and, in the present study, we perform a slice tomography to reconstruct the conductivity distribution in a cross-section limited by the ring of electrodes (Fig. 7). This approach is similar to the slice impedance tomography of the human thorax (Adler *et al.*, 2012) where the lung cavities provoke high contrasts of electrical conductiv-

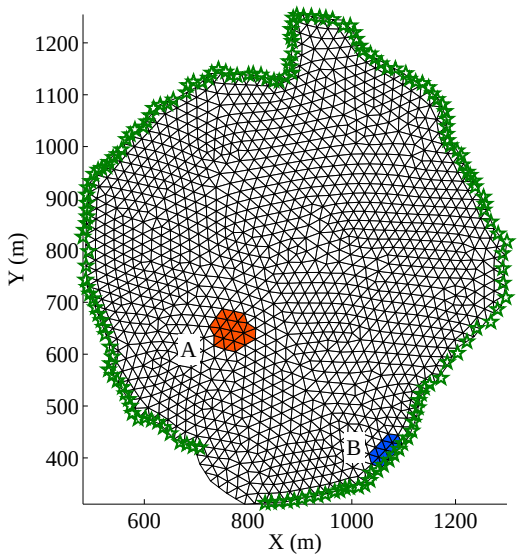

Figure 7. Meshing of the conductivity cross-section used in the SERT inversion. The green stars represent the electrodes. The orange and blue elements labelled A and B are used as examples to illustrate the construction of the 3D forward model shown in Fig. 5.

ity (Vogt *et al.*, 2012). In the present study, SERT is implemented by defining the unknown conductivity distribution $\sigma_{2\mathrm{d}}$ on a coarsely meshed 2D cross-section in order to reduce the number W of conductivity values to invert (Fig. 7).

The cross-section conductivity $\sigma_{2\mathrm{d}}$ is subsequently used to construct the full 3D conductivity distribution $\sigma_{3\mathrm{d}}$ necessary to solve a forward 3D finite element model (Fig. 5). This is achieved by using a coarse-to-fine $N \times W$ matrix $\mathbf{M}$ that maps the conductivity $\sigma_{2\mathrm{d}}$ of each element of the cross-section (Fig. 7) onto each of the N elements of the 3D model (Fig. 5). For elements vertically located either above or below the cross-section, the mapping is performed through a vertical extrusion that makes the conductivity distribution vertically invariant (i.e. 2.5D). This case is illustrated with the elements labelled A in Fig. 7 that gives the extruded vertical column A in the 3D model of Fig. 5. Elements located outside the extruded cross-section have their conductivity values assigned with a nearest neighbour criteria. This case is illustrated with the 3D elements labelled B in Fig. 5 whose conductivity is inherited from element B of the cross-section (Fig. 7). In the present study, the number of conductivity values $\sigma_{2\mathrm{d}}$ to invert is $W = 2690$ and $\sigma_{3\mathrm{d}}$ is defined on $33,174$ nodes forming the $N = 170,491$ elements of the 3D model (Fig. 5).

Both the forward modelling and the inversion are implemented with the open-source EIDORS software initially dedicated to medical applications (Polydorides & Lionheart, 2002; Adler & Lionheart, 2006) and recently augmented with geophysical functionalities (Lesparre *et al.*, 2013). The meshing is performed with NETGEN (Schöberl, 1997) and uses a digital elevation model with a mesh of 5 m (Fig. 5). Point electrodes are used to represent the steel rods used on the field. A refined meshing is implemented near the current electrodes to account for the sharp gradient of the electrical potential (Rücker *et al.*, 2006).

The forward model solution gives the electrical potential $u(x, y, z)$ which is further transformed into apparent resistivity $\tilde{\rho}_{app}$ for a given distribution of the electrical conductivity $\sigma(x, y, z)$. Insulating conditions are imposed on the boundaries Γ of the model volume Ω excepted at the current electrodes where a Neumann condition is imposed to represent the injected electrical current. The equations to be solved read,

$$\nabla \cdot (\sigma \nabla u) \; = \; -\nabla \cdot \mathbf{j} \;\text{in}\, \Omega \; \in \; \mathbb{R}^3, \tag{1}$$

$$\sigma \left(\frac{\partial u}{\partial n} \right) \; = \; \mathbf{j} \cdot \mathbf{n} \;\; \text{on}\, \Gamma. \tag{2}$$

where $\mathbf{j}$ is the source current density and $\mathbf{n}$ denotes the outward normal on Γ (Rücker *et al.*, 2006).

Because of the large range ($10 - 1000$ Ω.m) spanned by the apparent resistivity data, the fit is made on $\log(\tilde{\rho}_{app})$ instead of $\tilde{\rho}_{app}$. Inverted parameters correspond to log-conductivity which is the natural quantity that appears in the integral equation relating σ to V_k (Pessel & Gibert, 2003). Working in the log domain also makes the usage of either conductivity or resistivity equivalent (Tarantola, 2006), and it also appears in asymptotic formulations of high-contrast conductivity imaging as shown by Borcea *et al.* (1999) (Günther *et al.*, 2006; Marescot *et al.*, 2008; Lesparre *et al.*, 2013).

The inverse problem aims to recover the distribution of the logarithm of the conductivity $\boldsymbol{\varsigma} = (\varsigma_1, \varsigma_2, ..., \varsigma_K)^t$ in the cross-section able to reproduce the logarithm of the apparent resistivity data $\log \boldsymbol{\varrho} = (\log \varrho_1, \log \varrho_2, ..., \log \varrho_W)^t$. The inversion is iteratively performed with a conjugate gradient method. Although SERT strongly reduces the ill-posedness of the inversion, the inverse problem remains strongly underdetermined and a regularization of the Jacobian is performed through a filtering via a singular value decomposition (SVD) (Marescot *et al.*, 2008; Lesparre *et al.*, 2013). In practice, the SVD cut off used to construct the pseudo-inverse $\mathbf{J}^\dagger$ of the Jacobian is chosen according to an L-curve criterion (Hansen, 2001).

The main stages of the inversion procedure are:

1) Estimation of the 3D forward problem from a given distribution of $\boldsymbol{\varsigma}$: $\log \tilde{\boldsymbol{\varrho}}^i = f(\boldsymbol{\varsigma})^i$, with i the iteration number;
2) Computation of the Jacobian to estimate the data sensitivity to changes of the sought values defined by the coarse 2D mesh

$$J_{w,k} = \frac{\partial \log \tilde{\varrho}_w}{\partial \varsigma_k}; \tag{3}$$

3) The direction of the perturbation ($\boldsymbol{\delta}^i$) affected to the sought values is estimated from the SVD-regularized pseudo inverse of the Jacobian

$$\boldsymbol{\delta}^i = (\mathbf{J}^\dagger)^i (\log \boldsymbol{\varrho} - \log \tilde{\boldsymbol{\varrho}}^i); \tag{4}$$

4) Perturbations are then added to the previous values $\boldsymbol{\varsigma}^i$, with a step length α^i

$$\boldsymbol{\varsigma}^{i+1} \; = \; \boldsymbol{\varsigma}^i + \alpha^i \boldsymbol{\delta}^i; \tag{5}$$

5) Inverted values defined on the 2D coarse mesh $\boldsymbol{\varsigma}^i$ are interpolated using the matrix $\mathbf{M}$ to reconstruct the 3D forward model;
6) Computation of the 3D forward model with some trial

values for α^i in order to estimate the corresponding values of $\log \tilde{\boldsymbol{\varrho}}^{i+1}$:

$$\log \tilde{\boldsymbol{\varrho}}^{i+1} = f(\boldsymbol{\varsigma}^i + \alpha^i \boldsymbol{\delta}^i); \quad (6)$$

7) Residuals $\log \boldsymbol{\varrho} - \log \tilde{\boldsymbol{\varrho}}^i$ corresponding to the different values of α^i are compared to estimate the appropriate value for α^i, which retained value is the one corresponding to the minimum value of the second order polynomial fitting the trial points with a new distribution for $\boldsymbol{\varsigma}$.
8) If convergence is not achieved, return to step 1.

The starting model of the inversion is initialized with a resistivity of 106 Ω.m which corresponds to the average of the measured apparent resistivities. The first iteration is done with 13 trial values for α, varying between 0.2 and 0.5. For next iterations, the trial values correspond to $\frac{1}{2}\alpha^{i-1}$; α^{i-1} ; $2\alpha^{i-1}$, where α^{i-1} represent the step length used at the previous iteration. This procedure efficiently reduces the number of the forward model computations which is the most time-consuming part of the inversion (Marescot *et al.*, 2008). In practice, ten iterations are performed and the convergence is mainly obtained during the first two iterations.

2.3 Results

The resistivity cross-section σ_{2d} obtained from the SERT inversion of the data set shown in Fig. 6 is displayed in Fig. 8. Resistivity values span a range of 2 orders of magnitude, from 10 to 1000 Ω.m. The L-curve cut off used to obtain the results of Fig. 8 corresponds to a residual-to-roughness ratio $\lambda = 0.0077$, and the global root mean square error is about 20%.

The cross-section model of conductivity used in the inversion constitute an important simplification and only the main structures labelled R1 and C1 to C6 in the reconstructed cross-section shown in Fig. 8 are discussed hereafter. These structures remain stable during a sequence of independent inversions performed with different values of the control parameters (i.e. number of iterations, cut-off λ in the L-curve, meshing,...). These tests show that several structures located near the boundary of the cross-section may significantly vary both in size and conductivity contrast from one inversion to another. Such variations are typical of poorly resolved domains where non-uniqueness may produce the appearance of small-scale structures with opposite conductivity contrasts (i.e. one conductive and one resistive) nearby stable large-scale structures. This is for instance the case of the two resistive anomalies located on the western and southern sides of the R1 resistive structure (Fig. 8; Yasin *et al.*, (2011)).

3 INTERPRETATION OF MAIN STRUCTURES

3.1 Resistive ridge R1

Structure R1 is the only major resistive structure of the cross-section with an average resistivity of $\approx$ 400 Ω.m. The most resistive part of R1 is localized beneath the south western side of the lava dome and its northern end coincides with a series of promontories visible on the summit plateau, the most prominent being the Dolomieu peak located near the northern end of R1 (PD on Fig. 9). The R1

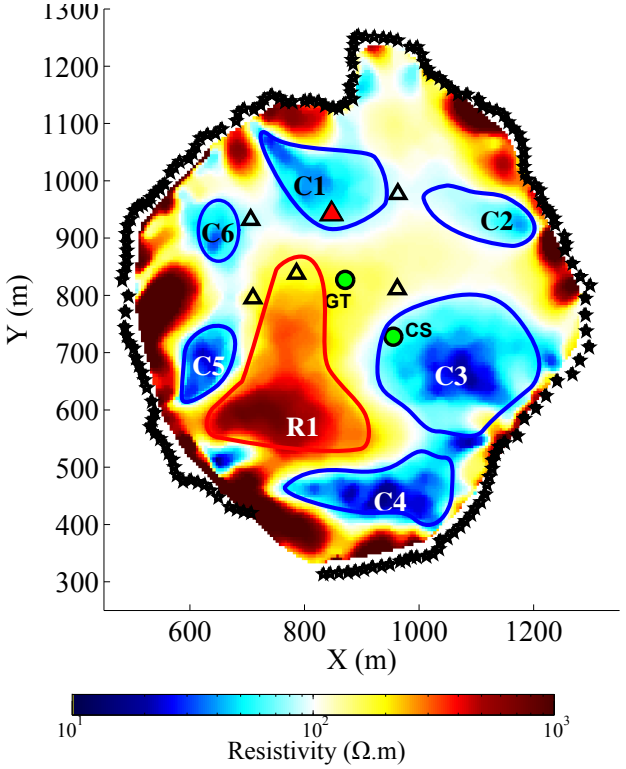

Figure 8. Electrical resistivity cross-section σ_{2d} obtained from the SERT inversion of the data set shown in Fig. 6. The black stars represent the electrode positions. The green circles correspond to acid ponds and triangles correspond to summits on the plateau at the top of La Soufrière. The highest summit La Découverte (1, 467 m) is marked with a red triangle.

structure is located beneath the 1D resistivity soundings L, M, O and P of Nicollin *et al.* (2006) who give a resistivity range of 230 $-$ 500 Ω.m for the basement of their 1D models. VLF soundings performed above the northern part of R1 by Zlotnicki *et al.* (2006) give a resistivity range of 90 $-$ 250 Ω.m. The agreement between the resistivity found for the R1 structure and those derived from geo-electrical soundings performed on the top part of the dome indicate that R1 corresponds to the root of a resistive body that vertically extends up to the summit of the lava dome. This *a posteriori* validates the vertically extruded resistivity model used in the present study.

The R1 structure also coincides with the dense region RS3 visible on the western side of the East-West muon radiography shown in the top part of Fig. 3. Both the high resistivity and density are typical of a massive lava body, and this agrees with the fact that the peaks visible at the summit are likely to be the top parts of extruded vertical lava spines. The southern half of R1 is curved eastward and may be associated with the deep part of a bulge located on the southern flank of the lava dome.

The R1 ridge seems to constitute an efficient barrier that prevents hydrothermal fluids to flow on the West side of the lava dome. This may explain the absence of any activity during the successive phreatic crises that punctuated the eruptive history of the volcano. However, the chemical tracing performed by Bigot *et al.* (1994) sustains the existence of an hydraulic pathway below the R1 structure and linking the *Tarissan* pit (GT on Fig. 9) to the *Bains Jaunes* hot springs

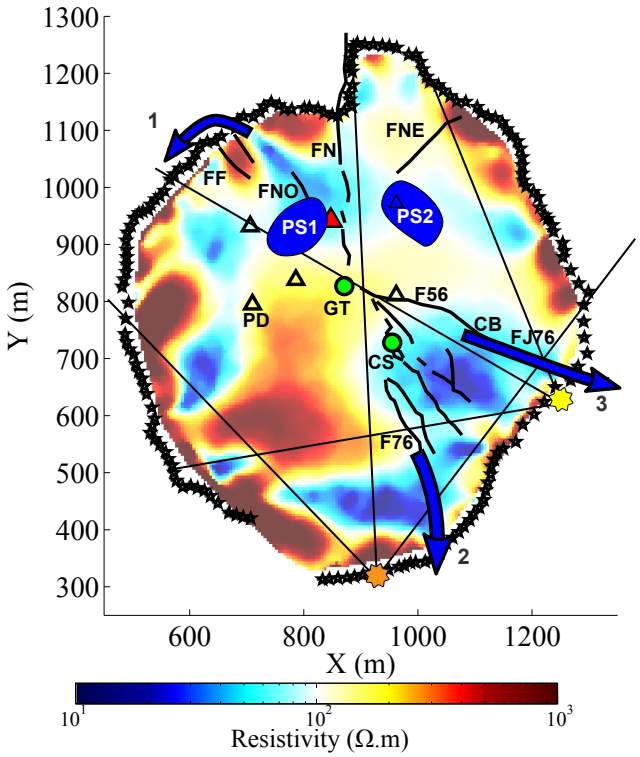

Figure 9. Reconstruction of the electrical resistivity at the dome base. Main geological structures are reported such as fractures (black lines), peaks (triangles) and acid ponds (green circles). The summit of La Soufrière is in red. Blue arrows correspond to water resurgence during historical phreatic eruptions (Feuillard *et al.*, 1983; Komorowski *et al.*, 2005). Blue areas show low voltages zones from self potential measurements (Zlotnicki *et al.*, 2006). The location of the telescope stations from which muon radiographies were obtained are also localized (yellow and orange stars), their corresponding line of sight as well as their aperture angle are reported too.

located about 1 km south-west of the dome. This indicates that the basis of the R1 body is probably highly fractured or altered below the lava dome.

3.2 Conductive structures C1 and C3

We join the interpretation of the C1 and C3 conductive structures (Fig. 8) because both are associated with major surface fractures that have been active during the 1976 – 1977 crisis such as *Fracture Faujas* (FF) under C1 and *Fracture 1956* (F56), *Fracture 8 juillet 1976* (FJ56), and *Fracture 30 août 1976* (F76) under C3 (Figs. 2 and 9; Komorowski *et al.*, 2005). These structures have an average resistivity of $\approx 50\ \Omega.\mathrm{m}$ in agreement with the C 1D sounding of Nicollin *et al.* (2006) who report a basement resistivity of $35\ \Omega.\mathrm{m}$ at the eastern edge of C3. The VLF sounding performed by Zlotnicki *et al.* (2006) in the same area give significantly higher resistivities in the $200 - 800\ \Omega.\mathrm{m}$ range. This discrepancy may be explained by the fact that VLF soundings are limited to shallow structures which, in the considered area, are constituted by rockfall deposits. C1 is in the axis of the low-density RF4 region of the *Roche Fendue* muon radiography (bottom of Fig. 3), and C3 corresponds to the low-density domain RS4 in the *Ravine Sud* radiography (top of Fig. 3). Both the low density and the low resistivity of C1 and C3 indicate that these regions are likely to be filled with altered unconsolidated material saturated with hydrothermal fluids.

Both C1 and C3 are associated with vent collapses that occurred during the explosive opening of fractures during historical eruptions. These events ejected a mass of non-juvenile debris from the dome that flowed for a short-run out in nearby valleys (Feuillard *et al.*, 1983; Sheridan, 1980; Komorowski *et al.*, 2005). The collapse associated with C1 lead to the *Faujas* rockslide that occurred on April 26^{th} 1798 during the $1797 - 1798$ phreatic eruption (FF on Fig. 9). Later, on February 12^{th} 1837, a new fracture opened nearby the *Faujas* rockslide and released a lahar (blue arrow 1 in Fig. 9) that invaded the *Ravine Amic*, a gully located on the north-west side of the dome (Fig. 2), and the *Noire* river (Hapel-Lachênaie *et al.*, 1798; Komorowski *et al.*, 2005). These events support the hypothesis that C1 is a reservoir likely to release significant amount of fluid and energy. The connection of C1 with surface fractures (*Fracture du Nord Ouest* (FNO) and *Fente du Nord* (FN) ; Figs. 2 and 9) is sustained by the presence of a negative anomaly of spontaneous potential (Zlotnicki *et al.*, 1994) typical of downward-going fluid flow. Although located in a presently inactive region of the summit plateau of La Soufrière, this reservoir seems still active as observed during the $1976 - 1977$ crisis when ephemeris vents appeared in several fractures.

The explosive collapse associated with C3 occurred on August 30^{th} 1976 during a particularly intense phreatic event where the *Tarissan* crater (GT on Fig. 9) erupted and ejected blocks of a few meters in diameter. This collapse released a lahar (blue arrow 2 in Fig. 9) that invaded the *Matylis* river. Another lahar occurred in the *Breislack* crater (CB, blue straight arrow labelled 3 in Fig. 9) and invaded the *Carbet* river (Feuillard *et al.*, 1983). These events occurred at three locations situated on the edge of the C3 structure and they may have been triggered by an overpressure of the corresponding reservoir. The westernmost part of the C3 structure is located beneath the presently active area of the summit plateau where intense vents (CS on Fig. 9) emit very acidic fluids of magmatic origin and that probably percolated through C3 which represents a large volume able to release a significant amount of energy and fluid. Moreover, this large volume of fluid is present in a particularly fractured and hydrothermally altered zone of the dome (Fig. 9).

3.3 Conductive structure C2

The C2 conductive structure is located in a presently inactive part of the lava dome. Its northern edge is limited by the *Fracture du Nord-Est* (FNE on Fig. 9) that was reported active at the end of the 17^{th} century during the 1680 eruption (Boudon *et al.*, 1988; Komorowski, 2008). No activity was reported on the summit plateau in this area during the 1956 and $1976 - 1977$ crisis, and only a moderate vent was observed at the eastern edge of C2 on the flank of the lava dome during the $1976 - 1977$ eruption. The fact that C2 remained inactive during the intense $1976 - 1977$ crisis can be a clue that the C2 reservoir is isolated from C1 and C3 by a hydrological barrier corresponding to the ridge of moderate resistivity (i.e. $\approx 100\ \Omega.\mathrm{m}$) visible on the southern and western sides of C2 (Fig. 9).

In November 2009, a moderate landslide (Fig. 1) occurred after several days with heavy rains on the eastern

Figure 10. Plastic bluish-gray hydrothermally-altered clay observed in landslide deposits.

extremity of C2. A clear negative anomaly of spontaneous potential (Zlotnicki *et al.*, 1994) is associated with C2 and supports the existence of a downward fluid flow from the summit plateau down to the C2 reservoir which is likely to be connected to the hot Carbet spring (blue point labelled CE in Fig. 2) and the Carbet-Echelle fumarolic field (label 6 on Fig. 2; Zlotnicki et al., 2006; Komorowski, 2008). Field observations of the landslide deposit and the landslide scar show the abundant and pervasive of plastic bluish-gray hydrothermally-altered clay-rich formations (Fig. 10) that form part of the internal units of the dome. These clay units are present *in situ* in the dome and constitute low-strength low-friction layers that promoted land-sliding following an exceptional intense rainfall event that occurred in 19^{th} and 20^{th} of November 2009 (Meteo France, 2009).

3.4 Conductive structures C4, C5 and C6

The conductive structures C4, C5 and C6 appear as peripheral structures not connected with the central regions of the dome. Their resistivity of $\approx 40\ \Omega.\text{m}$ agrees with the A, B and H 1D soundings of Nicollin *et al.* (2006) who find a resistivity of $\approx 30\ \Omega.\text{m}$ for the basement of their 1D models. The materials forming these structures are likely to be unconsolidated debris fallen from the steep slopes of the lava dome. This constitute potentially unstable volumes that may produce significant landslides during heavy rains or earthquakes.

4 CONCLUDING REMARKS

The data analysed in the present study are well-adapted to get information concerning the innermost resistivity structure of La Soufrière dome (Fig. 4). The reconstructed resistivity cross-section shows that the interior of the lava dome contains three main conductive domains (C1, C2, C3 in Fig. 8) and one resistive structure (R1 in Fig. 8).

Considering the resistivity values of these structures together with the densities obtained by cosmic muon radiography (Fig. 3) we may conclude that C1, C2 and C3 are reservoirs filled with unconsolidated material and conductive hydrothermal fluids. This description is coherent with the activity observed during the successive phreatic eruptions that occurred since the creation of the lava dome 500 years ago.

Similarly, R1 is interpreted as a massive lava body that vertically extends through the whole height of the lava dome and which seems to constitute a barrier that, up to now, blocked eruptive activity on the south-west flank of the volcano. However, the chemical tracing performed by Bigot *et al.* (1994) suggests that this barrier is fractured at least at its basis level.

The presently active reservoir C3 is located inside the south-eastern quarter of the dome and, accounting for the fact that both structures were active in $1976 - 1977$, a connection seems to exist with the C1 reservoir located in the north-western quarter. These two reservoirs may contain a significant amount of fluids and thermal energy that could be released in case of rapid deflation caused by landslide or over-heating at the base of the dome as was observed at several instances for Soufrière Hills at Montserrat since the beginning of the magmatic eruption in 1995 (Komorowski *et al.*, 2005). Oriented blasts and mud flows released by the reservoirs may invade nearby rivers – *Carbet*, *Matylis-Galion*, *Rivière Noire* – over several kilometres.

The C3 and C1 structures fall nearby the most important and historically active fractures that transect the dome in half. Moreover these structures are a continuous of the en-echelon normal *La Ty* fault (Fig. 2) that propagates from the south-east to the north-west through the *Fracture 30 août 1976* (F76 on C3 structure, Fig. 9), through the summit craters and fractures, and the *Fente du Nord* (FN on the eastern edge of the C1 structure, Fig. 9). La Soufrière lava dome is thus characterized by this heterogeneous geometry of low density and high-conductivity fluid-saturated and hydrothermally altered areas. The clear recurrent link of these structures to explosive historical activity and major surface deformation associated with recent phreatic and still-born magmatic eruptions suggest that areas within La Soufrière lava dome are prone to slope instability and partial edifice collapse, overpressurization leading to explosive vent fracturing, as well as the genesis of significant volume of water from acid perched hot aquifers that will generate mobile and potentially damaging mudflows (lahars). Hence these results have important implications for continuing multi-parameter monitoring of La Soufrière volcano, hazard scenario definition, risk assessment and crisis management.

ACKNOWLEDGMENTS

We benefited from the help of Florence Nicollin (Rennes

1 University) and colleagues from the Guadeloupe Volcano and Seismological Observatory (IPGP/OVSG) in acquiring the electrical resistivity measurements. Comments made by two anonymous referees helped us to improve the manuscript. The recent eruptive history of the volcano has been improved in the framework of the CASAVA ANR project. The EIDORS open-source software is available at `http://eidors3d.sourceforge.net`. The work of B. Grychtol was supported by a Research Fellowship from the Alexander von Humboldt Foundation. Financial support was provided by NSERC Canada. This is IPGP contribution ****.

REFERENCES

Adler, A. & Lionheart, W.R.B., 2006. Uses and abuses of EIDORS: An extensible software base for EIT, *Physiol. Meas.*, **27**, S25–S42.

Adler, A., Amato, M. B., Arnold, J. H., Bayford, R., Brown, B. H., Stenqvist, O., Weiler, N. & Wolf, G.K., 2012. Whither lung EIT: Where are we, where do we want to go and what do we need to get there?, *Physiol. Meas.*, **33**, 679.

Bigot, S., Boudon, G., Semet, M. P., & Hammouya, G., 1994. Traçage chimique de la circulation des eaux souterraines sur le volcan de la Grande Découverte (la Soufrière), Guadeloupe. *Comptes Rendus Acad. Sci.*, **319**, 1215–1221.

Boichu, M., Villemant, B., & Boudon, G., 2008. A model for episodic degassing of an andesitic magma intrusion. *J. Geophys. Res. Sol. Ea.*, **113**, 1978–2012.

Boichu, M., Villemant, B. & Boudon, G., 2011. Degassing at La Soufrière de Guadeloupe Volcano (Lesser Antilles) since the Last Eruptive Crisis in 1975-77: Result of a Shallow Magma Intrusion ?, *J. Volcanol. Geotherm. Res.*, **203**, 102–112.

Borcea, L., Berryman, J. G., & Papanicolaou, G. C., 1999. Matching pursuit for imaging high-contrast conductivity, *Inverse Problems*, **15**, 811–849.

Boudon, G., Semet, M.P. & Vincent, P.M., 1987. Magma and hydrothermally-driven sector collapses: the 3,100 and 11,500 B.P. eruptions of la Grande Découverte (La Soufrière) volcano, Guadeloupe, FrenchWest Indies. *J. Volcanol. Geotherm. Res.*, **33**, 317–323.

Boudon, G., Dagain, J., Semet, M. & Westercamp, D. (1988). Carte géologique à 1/20000e du Massif volcanique de la Soufrière, 1 sheet Notice explicative de la carte géologique 1/20000e du Massif volcanique de la Soufrière - Carte Géologique, BRGM-CNRS-DRM-IPGP, Editions BRGM, Orléans, 1-43

Boudon, G., Komorowski, J.C., Villemant, B. & Semet, M.P, 2008. A new scenario for the last magmatic eruption of La Soufrière of Guadeloupe (Lesser Antilles) in 1530 AD Evidence from stratigraphy radiocarbon dating and magmatic evolution of erupted products, *J. Volcanol. Geotherm. Res.*, **178**, 474–490.

Carrière, S.D., Chalikakis, K., Sénéchal, G., Danquigny, C., & Emblanch, C., 2013. Combining Electrical Resistivity Tomography and Ground Penetrating Radar to study geological structuring of karst Unsaturated Zone. *J. App. Geophys.*, **94**, 31–41.

Coutant, O., Bernard, M.L., Beauducel, F., Nicollin, F., Bouin, M.P. & Roussel, S., 2012. Joint inversion of P-wave velocity and density, application to La Soufrière of Guadeloupe upper geothermal system, Lesser Antilles, *Geophys. J. Int*., **191**, 723–742.

Feuillard, M., Allegre, C.J., Brandeis, G., Gaulon, R., Le Mouël, J.L., Mercier, J.C., Pozzi, J.P. & Semet, M.P. (1983). The 19751977 crisis of la Soufrière de Guadeloupe (FWI): A still-born magmatic eruption. *J. Volcanol. Geotherm. Res.*, **16**, 317–334.

Fournier, R.O., 2006. Hydrothermal systems and volcano geochemistry, in *Volcano Deformation*, Springer Berlin Heidelberg, 323–341.

Friedel, S., 2003. Resolution, stability and efficiency of resistivity tomography estimated from a generalized inverse approach, *Geophys. J. Int.*, **153**, 305–316.

Gibert, D., Beauducel, F., Déclais, Y., Lesparre, N., Marteau, J., Nicollin, F. & Tarantola, A., 2010. Muon tomography: plans for observations in the Lesser Antilles, *Earth Planets Space*, **62**, 153.

Gunawan, H., 2005. Gravimétrie et microgravimétrie appliquées à la volcanologie: exemples de la Soufrière de Guadeloupe et du Mérapi, Thèse de doctorat, Université Denis Diderot Paris 7, Paris.

Günther, T., Rücker, C. & Spitzer, K., 2006. Three-dimensional modelling and inversion of dc resistivity data incorporating topography–II. Inversion, *Geophys. J. Int.*, **166**, 506–517.

Hansen, P.C., 2001. The L-curve and its use in the numerical treatment of inverse problems, in: Johnston P, editor. *Comput. inverse probl. in electrocardiology*. Southampton: WIT Press. p 119–142.

Hapel-Lachênaie T.L.A., Peyre, A. & Fontelliau, C. (1798). Rapport fait aux citoyens Victor Hugues et Lebas, agents particuliers du directoire exécutif aux isles du vent, par la commission établie en vertu de leur arrêté du 12 vendémiaire, an 6 de la république, pour examiner la situation du Volcan de la Guadeloupe, et les effets de l'éruption qui a eu lieu dans la nuit du 7 au 8 du même mois. Au port de la Liberté - Guadeloupe. An VI. Reproduction de l'édition de 1798 par la Société d'Histoire De la Guadeloupe, Basse-Terre, 1977, 84 pp. + errata.

Komorowski, J.-C., Boudon, G., Semet, M.P., Beauducel, F., Anténor-Habazac, C., Bazin, S., Hammouya, G., 2005. Guadeloupe. In: Lindsay, J.M., Robertson, R.E.A., Shepherd, J.B., Ali, S. (Eds.), Volcanic Atlas of the Lesser Antilles. Seismic Research Unit, The University of the West Indies, Trinidad, pp. 65–102.

Komorowski, J.C., Legendre, Y., Caron, B. & Boudon, G., 2008. Reconstruction and analysis of sub-plinian tephra dispersal during the 1530 AD Soufrière (Guadeloupe) eruption: Implications for scenario definition and hazards assessment, *J. Volcanol. Geotherm. Res.*, **178**, 491–515.

Komorowski, J.C., 2008. Du volcan au pyroclaste: une approche pluridisciplinaire de la compréhension des processus éruptifs et de l'évaluation des aléas. Mémoire d'Habilitation à Diriger des Recherches, Université Denis Diderot Paris 7, spécialité: Sciences de la Terre, de l'environnement et des planètes, 549pp.

Le Friant, A.L., Boudon, G., Komorowski, J.C., Heinrich, P. & Semet, M.P., 2006. Potential flank-collapse of Soufrière Volcano, Guadeloupe, Lesser Antilles? Numerical simulation and hazards, *Nat. Hazards*, **39**, 381–393.

Legendre, Y., 2012. Reconstruction fine de l'histoire éruptive et scénarii éruptifs à la Soufrière de Guadeloupe : vers un modèle intégré de fonctionnement du volcan, Thèse de doctorat, Université Denis Diderot Paris 7, Paris.

Lesparre, N., Gibert, D., Marteau, J., Déclais, Y., Carbone, D. & Galichet E., 2010. Geophysical muon imaging: feasibility and limits, *Geophys. J. Int.*, **183**, 1348–1361.

Lesparre, N., Gibert, D., Marteau, J., Komorowski, J.C., Nicollin, F. & Coutant, O., 2012. Density Muon Radiography of La Soufrière of Guadeloupe: First Results and Comparison with Other Tomography Methods, *Geophys. J. Int.*, **190**, 1008–1019.

Lesparre, N., Gibert, D., Nicollin, F. & Adler, A., 2013. Monitoring the Excavation Damaged Zone by three dimensional reconstruction of the electrical resistivity, *Geophys. J. Int.*, **195**, 972–984.

Marescot, L., Palma Lopes, S., Rigobert, S. & Green A.G., 2008. Nonlinear inversion of geoelectric data acquired across 3D objects using a finite-element approach, *Geophysics*, **73**, 121–133.

Marteau, J., D. Gibert, N. Lesparre, F. Nicollin , P. Noli & Giacoppo, F., 2012. Muons tomography applied to geosciences and volcanology, *Nucl. Instr. Methods A*, **695**, 23–28.

Météo France, 2009. *Bulletin Climatologique Annuel 2009*, `http://www.meteo.gp/alaune/bca/archives/`.

Nicollin, F., Gibert, D., Beauducel, F., Boudon, G. & Komorowski, J.C., 2006. Electrical tomography of La Soufrière of Guadeloupe Volcano: Field experiments, 1D inversion and qualitative interpretation, *Earth Planet. Sc. Lett.*, **244**, 709–724.

Nicollin, F., Gibert, D., Beauducel, F., Boudon, G., & Komorowski, J. C., 2007. Reply to comment on Electrical Tomography of La Soufrière of Guadeloupe Volcano: Field experiments, 1D inversion and qualitative interpretation by N. Linde and A. Revil. *Earth Planet. Sc. Lett.*, **258**,

623–626.
Oldenburg, D.W., & Li, Y., 1999. Estimating depth of investigation in DC resistivity and IP surveys. *Geophysics*, **64**, 403-416.
Pessel, M. & Gibert, D., 2003. Multiscale electrical impedance tomography, *J. Geophys. Res.*, **108-B1**, 2054.
Polydorides, N. & Lionheart, W.R.B., 2002. A Matlab toolkit for three-dimensional electrical impedance tomography: a contribution to the Electrical Impedance and Diffuse Optical Reconstruction Software project, *Meas. Sci. Technol.*, **13**, 1871–1883.
Rücker, C., Günther, T. & Spitzer, K., 2006. Three-dimensional modelling and inversion of dc resistivity data incorporating topography I. Modelling, *Geophys. J. Int.*, **166**, 495–505.
Salaün, A., Villemant, B., Gérard, M., Komorowski, J.C. & Michel, A., 2011. Hydrothermal alteration in andesitic volcanoes: Trace element redistribution in active and ancient hydrothermal systems of Guadeloupe (Lesser Antilles) *J. Geochem. Explor.*, **111**, 59–83.
Samper, A., Quidelleur, X., Komorowski, J. C., Lahitte, P. & Boudon, G., 2009. Effusive history of the Grande Découverte Volcanic Complex, southern Basse-Terre (Guadeloupe, French West Indies) from new KAr CassignolGillot ages, *J. Volcanol. Geotherm. Res.*, **187**, 117–130.
Schöberl, J., 1997. NETGEN-an advancing front 2D/3D-mesh generator based on abstract rules, *Comput. Vis. Sci.*, **1**, 41–52.
Sheridan M.F., 1980. Pyroclastic block flow from the September, 1976, eruption of La Soufrière volcano, Guadeloupe, *Bull. Volcanol.*, **43**, 397–402
Tarantola, A., 2006. *Elements for physics*, Springer.
Villemant, B., Hammouya, G., Michel, A., Semet, M.P., Komorowski, J.C., Boudon, G. & Cheminée, J.L., 2005. The memory of volcanic waters: shallow magma degassing revealed by halogen monitoring in thermal springs of La Soufrière volcano (Guadeloupe, Lesser Antilles), *Earth Planet. Sc. Lett.*, **237**, 710–728.
Vogt, B., Pulletz, S., Elke, G., Zhao, Z., Zabel, P., Weiler, N., & Frerichs, I.,2012. Spatial and temporal heterogeneity of regional lung ventilation determined by electrical impedance tomography during pulmonary function testing. *Journal of Applied Physiology*, **113(7)**, 1154–1161.
Yasin, M., Böhm, S., Gaggero, P.O. & Adler, A., 2011. Evaluation of EIT system performance. *Physiol. meas.*, **32**, 851.
Zlotnicki, J., Feuillard, M., & Hammouya, G., 1994. Water circulations on La Soufrière volcano inferred by self-potential surveys (Guadeloupe, Lesser Antilles). Renew of volcanic activity?. *J. geomagn. geoelectr.*, **46**, 797–813.
Zlotnicki, J., Vargemezis, G., Mille, A., Bruère, F., & Hammouya, G., 2006. State of the hydrothermal activity of Soufriere of Guadeloupe volcano inferred by VLF surveys. *J. appl. geophys.*, **58**, 265–279.

APPENDIX A: COSMIC MUON RADIOGRAPHIES

Density radiography using cosmic muons is a novel method that uses the attenuation of the flux of muons crossing a geological body to determine its density structure (Gibert *et al.*, 2010). Measurements are made with telescopes equipped with detection matrices that allow to count the number of muons coming from about one thousand of lines of sight as shown in Fig. A1 (Marteau *et al.*, 2012). For each line of sight, the number of detected muons that crossed the volcano is compared with the incident flux in order to deduce the amount of matter – also called the opacity (in $\mathrm{g/cm^2}$) – encountered by the particles along their trajectory (Lesparre *et al.*, 2010). The opacity values are converted into average density along the lines of sight to produce the radiographies of Fig. 3.

One advantage of muon density radiography is the straight ray geometry of the acquisition (Fig. A1) which allows to locate the density heterogeneities visible on the radiographies. Because of the cone-like geometry of the rays, the density structures visible on Fig. 3 are averaged along more or less oblique lines of sight. The dotted lines visible on the radiographies bound the regions where the corresponding rays pass within ± 15 m above or below the electrode ring that defines the SERT cross-section of Fig. 7.

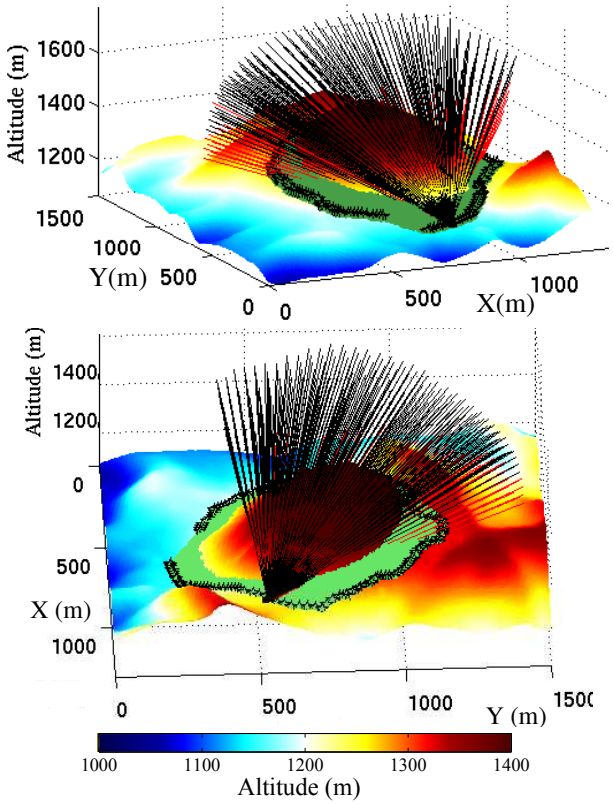

Figure A1. View of the lines of sight scanned by the cosmic muon telescope when located at *Ravine Sud* (top, altitude 1168 m) and *Roche Fendue* (bottom, altitude 1263 m). The data acquired at the *Ravine Sud* station produced the east-west radiography shown in the top part of Fig. 3, and the north-south radiography for the data of *Roche Fendue* is shown at the bottom of Fig. 3. The black stars represent the electrodes and the green surface represent the regions sounded by the SERT. The lines of sight that appear in red are entirely comprised in a volume of ± 15 m above and below the SERT cross-section. See Lesparre *et al.* (2012) for a detailed description of the muon tomography experiments on La Soufrière.